Using the motion of S2 to constrain vector clouds around SgrA

A Foschi, R Abuter, K Abd El Dayem, N Aimar, P. Amaro Seoane, A Amorim, J.P Berger, H Bonnet, G Bourdarot, W Brandner, et al.

Monthly Notices of the ROYAL ASTRONOMICAL SOCIETY

MNRAS **530,** 3740–3751 (2024)
Advance Access publication 2024 March 29

https://doi.org/10.1093/mnras/stae423

Using the motion of S2 to constrain vector clouds around Sgr A*

GRAVITY Collaboration: A. Foschi [1,2★] R. Abuter,[3] K. Abd El Dayem,[4] N. Aimar,[4] P. Amaro Seoane,[5,6,7,8] A. Amorim,[1,9] J. P. Berger [10] H. Bonnet,[3] G. Bourdarot,[5] W. Brandner [11] R. Davies,[5] P. T. de Zeeuw,[12] D. Defrère,[13] J. Dexter,[14] A. Drescher,[5] A. Eckart,[15,16] F. Eisenhauer,[5] N. M. Förster Schreiber,[5] P. J. V. Garcia,[1,2★] R. Genzel,[5,17] S. Gillessen,[5] T. Gomes,[1,2] X. Haubois,[18] G. Heißel,[4,19] Th. Henning,[11] L. Jochum,[18] L. Jocou,[11] A. Kaufer,[18] L. Kreidberg,[11] S. Lacour,[4] V. Lapeyrère,[4] J.-B. Le Bouquin,[10] P. Léna,[4] D. Lutz,[5] F. Mang,[5] F. Millour,[20] T. Ott,[5] T. Paumard,[4] K. Perraut,[10] G. Perrin,[4] O. Pfuhl,[3,5] S. Rabien,[5] D. C. Ribeiro,[5] M. Sadun Bordoni,[5] S. Scheithauer,[11] J. Shangguan,[5] T. Shimizu,[5] J. Stadler,[5,21] C. Straubmeier,[15] E. Sturm,[5] M. Subroweit,[15] L. J. Tacconi,[5] F. Vincent,[4] S. von Fellenberg[5,16] and J. Woillez[3]

Affiliations are listed at the end of the paper

Accepted 2024 February 5. Received 2024 January 30; in original form 2023 December 6

ABSTRACT

The dark compact object at the centre of the Milky Way is well established to be a supermassive black hole with mass $M_\bullet \sim 4.3 \times 10^6\,\mathrm{M}_\odot$, but the nature of its environment is still under debate. In this work, we used astrometric and spectroscopic measurements of the motion of the star S2, one of the closest stars to the massive black hole, to determine an upper limit on an extended mass composed of a massive vector field around Sagittarius A∗. For a vector with effective mass $10^{-19} \lesssim m_\mathrm{s} \lesssim 10^{-18}$ eV, our Markov chain Monte Carlo analysis shows no evidence for such a cloud, placing an upper bound $M_\mathrm{cloud} \lesssim 0.1\%\, M_\bullet$ at 3σ confidence level. We show that dynamical friction exerted by the medium on S2 motion plays no role in the analysis performed in this and previous works, and can be neglected thus.

Key words: black hole physics – gravitation – celestial mechanics – Galaxy: centre – dark matter.

1 INTRODUCTION

Since the star S2 has been discovered orbiting the Galactic Centre (GC; Schödel et al. 2002; Ghez et al. 2003; Gillessen et al. 2009, 2017), its orbital motion has been largely and extensively used to constrain the properties of the supermassive black hole (SMBH) Sagittarius A* (Sgr A*) and the environment around it. S2 is part of the so-called S-cluster, which currently counts up to tens of detected stars (Sabha et al. 2012; Habibi et al. 2017; GRAVITY Collaboration 2022b).

The astrometric and spectroscopic data collected by two independent groups showed that the dynamics of S-stars is entirely dominated by the presence of a compact source with $M_\bullet \sim 4.3 \times 10^6\,\mathrm{M}_\odot$ at a distance of $R_0 \sim 8.3$ kpc. There is overwhelming evidence that the compact source is an SMBH (Schödel et al. 2002; Ghez et al. 2008; Genzel, Eisenhauer & Gillessen 2010; GRAVITY Collaboration 2019b, 2022a; Genzel 2021). Very strong arguments that the central dark mass is indeed an SMBH come from the measurement of the Schwarzschild precession in the orbit of S2 (GRAVITY Collaboration 2020), from the observations of near-infrared (IR) flares in correspondence with the innermost circular orbit of the SMBH (GRAVITY Collaboration 2018; Abuter et al. 2023) and by the image released by the Event Horizon Telescope Collaboration, which is compatible with the expected image of a Kerr black hole (BH; Akiyama et al. 2022).

The physics of horizons is so puzzling that any further evidence for their existence is welcome and provides important information on the scales at which new physics sets in. Currently, it is challenging to use orbits of S-stars around the GC to test the nature of the compact source itself and to distinguish it from other possible models, such as boson stars, dark matter (DM) cores, or wormholes, which have similar features to BHs (Amaro-Seoane et al. 2010; Grould et al. 2017a; Boshkayev & Malafarina 2019; De Della Monica & de Martino 2022; Laurentis, De Martino & Della Monica 2023). Note, however, that the optical appearance of hotspots (or stars) close to the accretion zone of Sgr A* may differ significantly should a horizon be absent (Rosa et al. 2022).

Equally important is the nature of the environment around SMBHs, in particular around Sgr A*. DM is expected to cluster at the centre of galaxies leading to 'overdensities' (Gondolo & Silk 1999; Sadeghian, Ferrer & Will 2013), which might leave an imprint in the motion of stars. S-stars are currently the main observational tool we have to look into this inner region of our Galaxy and thus they must be exploited to gain as much information as possible from their motion. For this and other reasons, the possibility of an extended

★ E-mail: arianna.foschi@tecnico.ulisboa.pt (AF), pgarcia@fe.up.pt (PJVG)

mass distribution around Sgr A* has been studied (Lacroix 2018; Bar et al. 2019; GRAVITY Collaboration 2022a; Heißel et al. 2022; Foschi et al. 2023). Specifically, GRAVITY Collaboration (2022a) derived an upper limit of $\delta M \sim 4000\,\mathrm{M}_\odot \sim 0.1\%\, M_\bullet$ for a density distribution described by a Plummer profile with length-scale $a_0 = 0.3$ arcsec.

A special, and interesting, model for DM concerns ultralight bosons. These arise in a variety of scenarios, for instance, the 'string axiverse' (Arvanitaki et al. 2010; Arvanitaki & Dubovsky 2011; Marsh 2016) or as a hidden U(1) gauge boson, a generic feature of extensions of the Standard Model (Goodsell et al. 2009; Jaeckel & Ringwald 2010). In fact, such fields can exist and grow even if they are only a minute component of DM, as they are amplified via a mechanism known as BH superradiance (Brito, Cardoso & Pani 2015b). In this process, the light boson extracts rotational energy away from the spinning BH, depositing it in a 'bosonic cloud', which can acquire a sizeable fraction of the BH mass. For a fundamental boson of mass m_s, the key parameter controlling the superradiant growth and energy extraction is the mass coupling $\alpha = M_\bullet m_\mathrm{s}$.

In a recent work (Foschi et al. 2023), we investigated the possibility that a massive scalar field clusters around Sgr A* in the form of a cloud (GRAVITY Collaboration 2019a). We showed that for the range of (dimensionless) mass couplings, $0.01 \lesssim \alpha \lesssim 0.045$ (which corresponds to a mass of the scalar field of $6 \times 10^{-19} \lesssim m_\mathrm{s} \lesssim 3 \times 10^{-18}$ eV), we are able to constrain the mass of the cloud to be $M_\mathrm{cloud} \lesssim 0.1\%\, M_\bullet$, recovering the upper bound found in GRAVITY Collaboration (2022a).

Here, we focus on a similar system: a massive vector cloud. As scalar fields, massive vector fields can form bound states around Kerr BHs, giving rise to stationary clouds. At the linear level and using the small coupling approximation, it has been shown that the superradiant instability is triggered on a time-scale $\tau_1 \propto \alpha^{-7}$ for vector clouds when compared to the scalar case of $\tau_1 \propto \alpha^{-9}$ (Pani et al. 2012; Brito et al. 2015b; Endlich & Penco 2017; Cardoso et al. 2018). Hence vector clouds grow much faster than their scalar counterparts and the field's mass m_s needed to make them grow in a time-scale smaller than the cosmic age is much smaller, making them more likely to be observed.

In this work, we will use the astrometric and spectroscopic data of star S2 collected at the Very Large Telescope (VLT) to constrain the fractional mass of a possible vector cloud around Sgr A*.

We will use units where $\hbar = c = G = 1$, unless otherwise stated.

2 SET-UP

In this work, we consider a massive vector field A_μ described by the Lagrangian,

$$\mathcal{L} = -\frac{1}{4} F_{\mu\nu} F^{\mu\nu} - \frac{1}{2}\mu^2 A_\mu A^\mu, \tag{1}$$

and A^μ satisfies the Proca equation of motion $D_\mu F^{\mu\nu} = \mu^2 A^\nu$. If the Compton wavelength of the vector field is much larger than the Schwarzschild radius $r_\mathrm{g} = M_\bullet$, the bound states of the field oscillate with frequency $\omega_\mathrm{f} \simeq \mu$ and can be written as (Baryakhtar, Lasenby & Teo 2017)

$$A^\mu(t, x) = \frac{1}{\sqrt{2\mu}} \left(\Psi^\mu(x)\, \mathrm{e}^{-\mathrm{i}\omega_\mathrm{f} t} + \mathrm{c.c.}\right). \tag{2}$$

In the limit $r \gg r_\mathrm{g}$, the Proca equation becomes a Schröedinger-like equation, and the Ψ_0 component can be expressed in terms of Ψ_i. Since the radial part of the potential is spherically symmetric, Ψ_i can be decomposed as

$$\Psi_i = R^{n\ell}(r) Y_i^{\ell, jm}(\theta, \phi), \tag{3}$$

where the $Y_i^{\ell, jm}(\theta, \phi)$ are the so-called pure-orbital vector spherical harmonics (Thorne 1980; Santos et al. 2020).

The fundamental mode of the field, which is also the mode that grows fastest due to superradiant mechanisms (Baryakhtar et al. 2017), is given by $\ell = 0$, $m = j = 1$, and $n = 0$. At leading order in α we can neglect A_0 and consider only the spatial components of the field, which can be written as (Chen et al. 2023)

$$A_i^{1011} = \Psi_0\, \mathrm{e}^{-\frac{\alpha^2 r}{M_\bullet}} (\cos(\mu t), \sin(\mu t), 0)\,. \tag{4}$$

From this profile, we can compute the energy–momentum tensor (Herdeiro, Radu & Rúnarsson 2016) and take the Newtonian limit, i.e. neglecting all the spatial derivatives and assuming a real field, obtaining

$$\rho = \frac{\Psi_0^2 \alpha^2}{M_\bullet^2}\, \mathrm{e}^{-\frac{2\alpha^2 r}{M_\bullet}}, \tag{5}$$

which coincides with the expression in Chen et al. (2023).

As done in Foschi et al. (2023), we can integrate the energy density in equation (5) to relate the amplitude of the field Ψ_0 with the mass of the vector cloud:

$$M_\mathrm{cloud} = \frac{\pi \Psi_0^2 M_\bullet}{\alpha^4}. \tag{6}$$

From the energy density in equation (5), we can get the potential generated by the cloud solving Poisson's equation: $\nabla^2 U_V = 4\pi\rho$ and using the spherical harmonic decomposition of Poisson & Will (2012) to get

$$U_V = \frac{\Lambda}{r}\left(M_\bullet - \mathrm{e}^{-2r\alpha^2/M_\bullet}\left(M_\bullet + r\alpha^2\right)\right), \tag{7}$$

where we have defined $\Lambda = M_\mathrm{cloud}/M_\bullet$.

2.1 Effects of the cloud on S2 orbit with osculating elements

We start our analysis of the effects of vector cloud on S2 motion using the method of osculating elements that can be found in Poisson & Will (2012). The basic idea is to treat the effect of the vector cloud as a perturbation of the Newtonian acceleration, assuming that the Keplerian description of the orbit is still approximately true. In this way, we are able to express the equations of motion in terms of the Keplerian elements $(e, a, i, \omega, \Omega, \mathcal{M}_0)$ (eccentricity, semimajor axis, inclination, argument of the periastron, longitude of the ascending node, and mean anomaly at epoch, respectively), which would be constant in a pure Newtonian set-up, and see how the perturbing force modifies them. In order to do so, we introduce a vectorial basis adapted to the orbital motion of the binary system BH–S2: $(\boldsymbol{n}, \boldsymbol{\lambda}, \boldsymbol{e}_z)$, where $\boldsymbol{n} = \boldsymbol{r}/r$, $\boldsymbol{e}_z = \boldsymbol{h}/h$ with $\boldsymbol{h} := \boldsymbol{r} \times \boldsymbol{v}$, and $\boldsymbol{\lambda}$ is orthogonal to both $\boldsymbol{n}$ and $\boldsymbol{e}_z$. We also assume that the mass of the star is negligible compared to the BH mass $M_\bullet$.

The perturbing force can be decomposed as

$$\boldsymbol{f} = \mathcal{R}\boldsymbol{n} + \mathcal{S}\boldsymbol{\lambda} + \mathcal{W}\boldsymbol{e}_z. \tag{8}$$

The variation of the orbital elements in terms of the perturbing force components is given in Kopeikin, Efroimsky & Kaplan (2011) and Poisson & Will (2012) and we report it for completeness in Appendix A.

Once the variation in time of the orbital elements is known, one can compute the secular change of the orbital element μ^a over a

complete orbit using

$$\Delta\mu^a = \int_0^{2\pi} \frac{\mathrm{d}\mu^a}{\mathrm{d}\phi}\,\mathrm{d}\phi, \tag{9}$$

where

$$\frac{\mathrm{d}\mu^a}{\mathrm{d}\phi} = \frac{\mathrm{d}\mu^a}{\mathrm{d}t}\frac{\mathrm{d}t}{\mathrm{d}\phi} \tag{10}$$

and

$$\frac{\mathrm{d}\phi}{\mathrm{d}t} = \sqrt{\frac{M_\bullet}{a^3(1-e^2)^3}}(1+e\cos\phi)^2. \tag{11}$$

2.1.1 *Effect of the vector cloud alone*

Because of the spherical symmetry of the energy distribution in equation (5), the only non-zero component of $\boldsymbol{f}_V$ is the radial one:

$$\mathcal{R}_V = \frac{\Lambda}{M_\bullet r^2}\left[-M_\bullet^2 + \mathrm{e}^{-2r\alpha^2/M_\bullet}\left(M_\bullet^2 + 2M_\bullet r\alpha^2 + 2r^2\alpha^4\right)\right], \tag{12}$$

while $\mathcal{S}_V = \mathcal{W}_V = 0$.

2.1.2 *Inclusion of the 1PN correction*

Since the Schwarzschild precession has been detected at 8σ confidence level by the GRAVITY Collaboration (2020, 2022a), it is interesting to see how the previous results change if we include the first post-Newtonian (PN) correction to the equations of motion.

This corresponds to having a total acceleration

$$\boldsymbol{a} = -\frac{M_\bullet \boldsymbol{r}}{r^3} + \boldsymbol{a}_V + \boldsymbol{a}_{1\mathrm{PN}}, \tag{13}$$

where

$$\boldsymbol{a}_{1\mathrm{PN}} = \frac{M_\bullet}{r^2}\left[\left(\frac{4M_\bullet}{r} - v^2\right)\frac{\boldsymbol{r}}{r} + 4\dot{r}\boldsymbol{v}\right], \tag{14}$$

with $\boldsymbol{r} = r\hat{r}$, $\boldsymbol{v} = \left(\dot{r}\hat{r}, r\dot{\theta}\hat{\theta}, r\dot{\phi}\sin\theta\hat{\phi}\right)$, and $v = |\boldsymbol{v}|$.

The decomposition of the acceleration in equation (14) into the basis $(\boldsymbol{n}, \boldsymbol{\lambda}, \boldsymbol{e}_z)$ has been done in Poisson & Will (2012) and here we report the result:

$$\mathcal{R}_{1\mathrm{PN}} = \frac{M_\bullet}{r^2}\left(4\dot{r}^2 - v^2 + 4\frac{M_\bullet}{r}\right), \tag{15}$$

$$\mathcal{S}_{1\mathrm{PN}} = \frac{M_\bullet}{r^2}\left(4\dot{r}r\dot{\phi}\right), \tag{16}$$

and $\mathcal{W}_{1\mathrm{PN}} = 0$. In order to express everything in terms of the orbital elements, we need to use the expressions for r, $\dot{r}$, and $\dot{\phi}$ reported in section 10.1.3 of Poisson & Will (2012).

In this second case, we set $\Lambda = 10^{-3}$, which corresponds to the current upper limit obtained by the GRAVITY Collaboration for the fractional mass of an extended mass distribution around Sgr A* (GRAVITY Collaboration 2022a; Foschi et al. 2023).

2.2 Data

The set of available data D is the same as in Foschi et al. (2023).

2.3 Fitting approach

The next step is to obtain a best-fitting value for the fractional mass Λ for different coupling α values. The procedure followed in this work is exactly the same as the one reported in Foschi et al. (2023). Specifically, we solve the equations of motion in equation (13) using the initial conditions reported in Appendix B. The solutions of this set of equations are given in the BH reference frame and must be projected into the observer reference frame using the three Euler angles Ω, i, and ω.

Following Grould et al. (2017b) we can define a new reference frame $\{x', y', z_{\mathrm{obs}}\}$ such that $x' = \mathrm{Dec.}$, $y' = \mathrm{RA}$ are the collected astrometric data, z_{obs} points towards the BH, and $v_{z_{\mathrm{obs}}}$ corresponds to the radial velocity (see Appendix C for details about how to perform the rotation of the reference frame).

Moreover, it is true that S2 motion happens mostly in a Newtonian regime, i.e. with $v \ll 1$, but near the periastron, it reaches a total space velocity $v \sim 10^{-2}$. In this region, relativistic effects become important and cannot be neglected. For this reason, we correct the radial velocity coming from equation (13), including both the relativistic Doppler shift and the gravitational redshift (Abuter et al. 2018).

Finally, we also consider the so-called Rømer delay, which is the difference between the observational dates and the actual emission dates of the signal due to the finite speed of light. Details about how to include Rømer delay and relativistic effects are reported in Appendix D.

For any given value of α, we fit for the following set of parameters:

$$\Theta_i = \{e, a, \Omega, i, \omega, t_{\mathrm{p}}, R_0, M_\bullet, x_0, y_0, v_{x_0}, v_{y_0}, v_{z_0}, \Lambda\}. \tag{17}$$

The additional parameters $\{x_0, y_0, v_{x_0}, v_{y_0}, v_{z_0}\}$ characterize the NACO/SINFONI data reference frame with respect to Sgr A* (Plewa et al. 2015). We refer the reader to Appendix E for more details about the Markov chain Monte Carlo (MCMC) implementation.

3 RESULTS

3.1 Variation of the orbital elements

In Fig. 1, we show the variation of the orbital elements $\Delta\mu^a/\Lambda$ due to the presence of the vector cloud for different values of the coupling α, as described in Section 2.1. The secular change is negligible for both the eccentricity e and the semimajor axis a.

The change in the mean anomaly at epoch $\mathcal{M}_0$ is instead proportional to α, increasing monotonically. $\mathcal{M}_0$ is directly related to the time of pericentre passage t_{p}: a larger mean anomaly at the epoch corresponds to a later pericentre passage.

The only meaningful change in the orbital elements is found in $\Delta\omega$, which quantifies the precession effect on the orbit, with ω the argument of pericentre. First of all, we observe that $\Delta\omega < 0$ always. This is a consequence of the fact that the presence of an extended mass within the orbit of S2 would produce a retrograde precession of the orbit (Heißel et al. 2022).

Unsurprisingly, its maximum variation is found in the range

$$0.003 \lesssim \alpha \lesssim 0.03. \tag{18}$$

Indeed, as in the case of scalar clouds (Foschi et al. 2023), this behaviour is expected if we compute the effective peak position of the energy distribution in equation (5),

$$R_{\mathrm{peak}} = \frac{\int_0^\infty \rho r\,\mathrm{d}r}{\int_0^\infty \rho\,\mathrm{d}r} = \frac{M_\bullet}{2\alpha^2}, \tag{19}$$

which, for the values of α reported in equation (18), corresponds to $5\times10^2 \lesssim R_{\mathrm{peak}} \lesssim 5\times10^4\,M_\bullet$, i.e. it roughly matches the orbital range of S2 ($3\times10^3 \lesssim r_{\mathrm{S2}} \lesssim 5\times10^4\,M_\bullet$). This result shows that the maximum variation in ω is found when the star crosses regions of higher (vector) density, while its orbit remains basically unaffected if the cloud is located away from its apoastron or too close to the central BH mass.

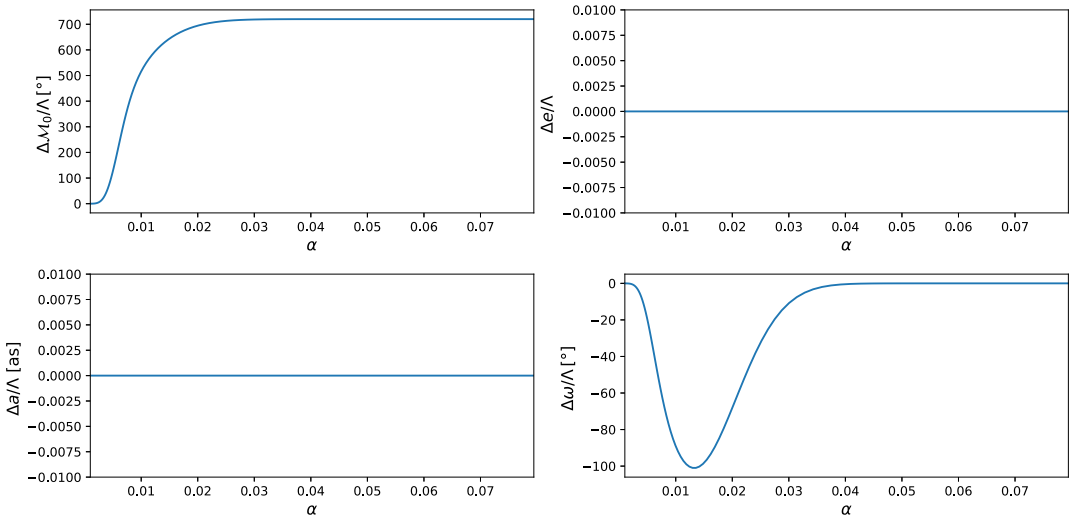

Figure 1. Variation of the orbital elements $\Delta\mu^a/\Lambda$ over an entire orbit for different values of the coupling constant α when only the vector cloud is present. The maximum variation in $\Delta\omega/\Lambda$ is roughly found in the range $0.003 \lesssim \alpha \lesssim 0.03$.

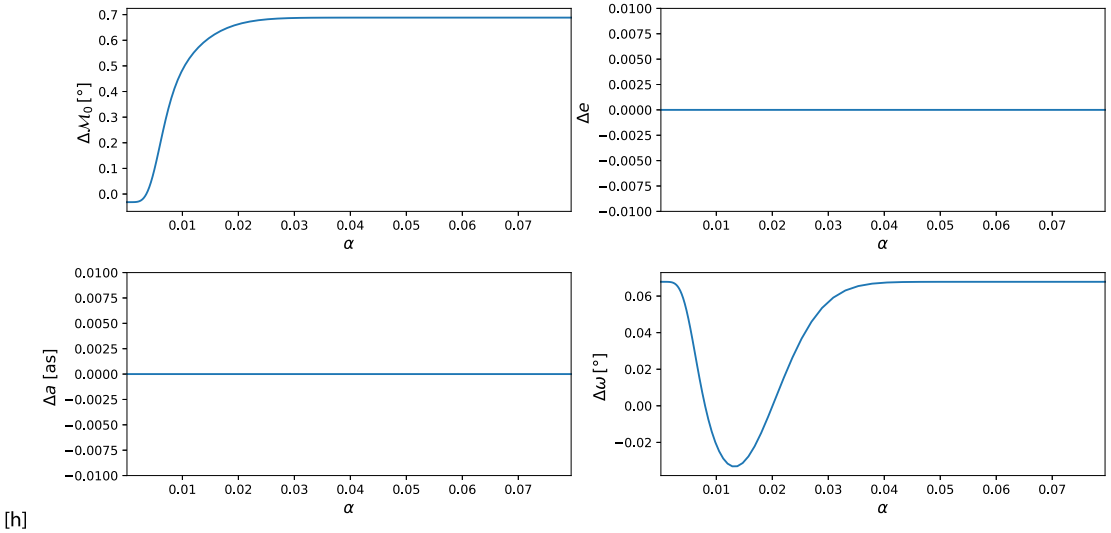

[h]

Figure 2. Variation of the orbital elements $\Delta\mu^a$ over an entire orbit for different values of the coupling constant α when one includes the Schwarzschild precession in the equation for the osculating elements. Here $\Lambda = 10^{-3}$. The maximum variation is still found in $0.003 \lesssim \alpha \lesssim 0.03$.

In Fig. 2, we show the variation of the orbital elements when the 1PN correction is included in the equations of motion, as described in Section 2.1.2. Opposite to the previous case, here, the variation of the argument of the pericentre $\Delta\omega$ can be either positive or negative, according to the value of α. Indeed now the retrograde precession induced by the vector cloud is compensated by the (prograde) Schwarzschild precession due to the 1PN correction in the equations of motion, and its maximum value corresponds to $\Delta\omega \simeq -1.8$ arcmin, which is smaller than the previous case with $\Lambda = 10^{-3}$ ($\Delta\omega \simeq -6$ arcmin).

3.2 Limit on the fractional mass Λ

Before running the MCMC algorithm we determine the initial guesses for the parameters listed in equation (17). We performed a simple χ^2 minimization using the PYTHON package LMFIT.MINIMIZE (Newville et al. 2016) with Levenberg–Marquardt method. In Fig. 3, we report the best-fitting values of Λ with relative 1σ uncertainties, and we compare the range of α with the effective peak position of the cloud in equation (19). The smallest uncertainties for Λ are found roughly in the range of equation (18), which is slightly different from the scalar cloud case (Foschi et al. 2023) and in agreement with the orbital variation reported in Fig. 2.

After performing the MCMC analysis, we look for the maximum likelihood estimator (MLE) $\hat{\Lambda}$, which in this case corresponds to the value that maximizes the posterior density distribution reported in Fig. 4, as a consequence of using flat priors and a Gaussian likelihood.

In Table 1, we report the values of $\hat{\Lambda}$ with relative 1σ uncertainties together with the value of the Bayes factor $\log K$. The latter is obtained by computing the marginal likelihoods by making use of the PYTHON package MCEVIDENCE developed in Heavens et al. (2017) and it is defined as $K = P(D|M_\alpha)/P(D|M_0)$, where M_α represents the BH plus vector cloud model, while M_0 corresponds to the non-perturbative one.

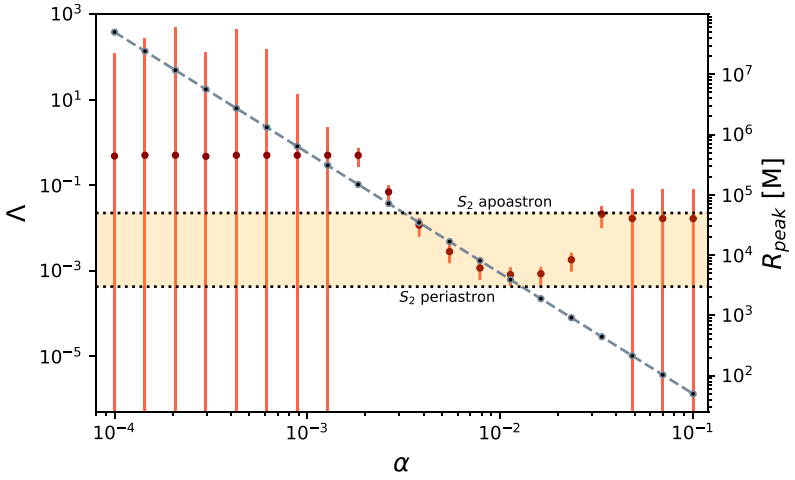

Figure 3. Best-fitting values for Λ and relative 1σ uncertainties as function of the coupling α obtained minimizing the χ^2. The grey dashed line represents the effective peak position of the vector cloud given by equation (19), while the orange band gives the orbital range of S2.

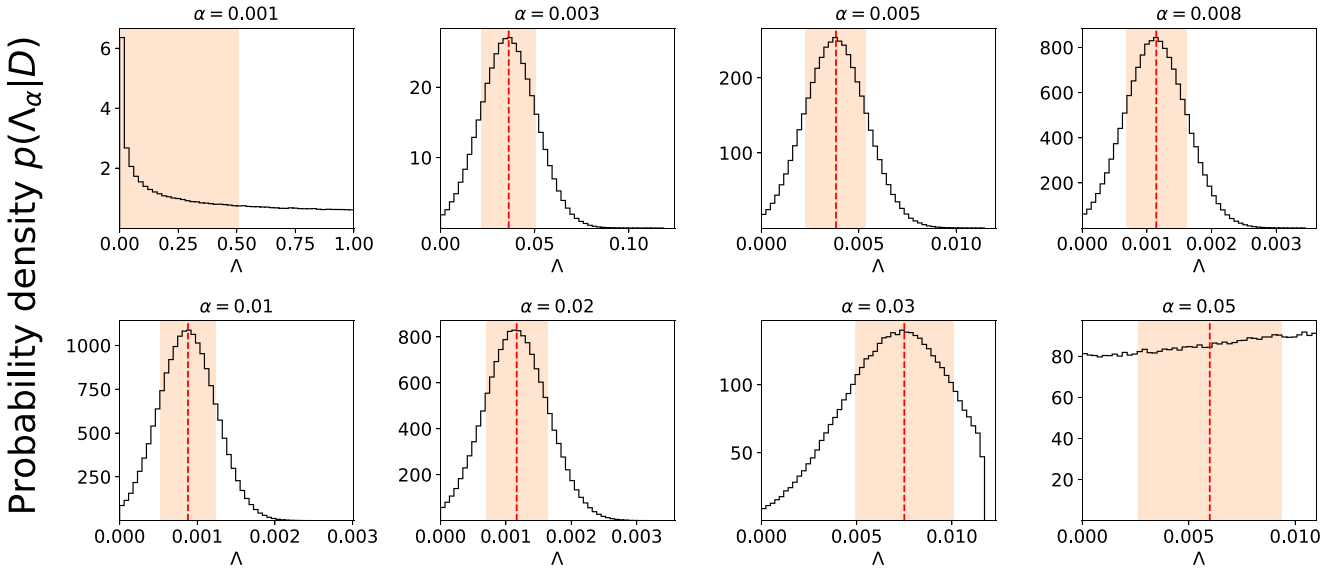

Figure 4. Posterior probability densities $p(\Lambda_\alpha|D)$ for different values of α. Red dashed lines represent the mean value of the distributions (which coincides with the MLE $\hat{\Lambda}$), while orange bands correspond to 1σ confidence level, such that ≈68 per cent of $p(\Lambda_\alpha|D)$ lies in that region.

When the posterior distribution is found to be non-normal and peaked at zero, we estimated the 1σ (3σ) confidence interval looking for that value of Λ such that roughly the 68% (99%) of $p(\Lambda|D)$ lies below that value. When $\alpha \gtrsim 0.3$, the distribution of Λ start to be flat, with a sudden drop around $\Lambda \simeq 10^{-2}$. One can show that for flat distributions in an interval $[a, b]$, the mean is given by $(a - b)/2$, while the variance is $(b - a)^2/12$ (Bailer-Jones 2017). We report those values in Table 1. However, what is important to notice in these cases is that for $\alpha \gtrsim 0.03$ ($R_{\rm peak} \lesssim 550\, M_\bullet$), it is not possible to determine a unique value for Λ that best fits the data, confirming the expectation from the χ^2 minimization.

When α is in the range of equation (18) the posterior distributions of Λ are Gaussian whose means and standard deviations are reported in Table 1. For all cases considered in this range, $\hat{\Lambda} \sim 10^{-3}$ with 1σ uncertainties roughly of the same order of magnitude. This makes all the $\hat{\Lambda}$ values derived from the MCMC analysis compatible with zero within the 3σ confidence level. In addition to this, the associated Bayes factors always have $\log K < 2$. This result, according to the literature (Kass & Raftery 1995), shows no statistical evidence in favour of the BH plus vector cloud model with respect to the non-perturbative case where no cloud is present. Hence we derive an upper limit of $\Lambda \lesssim 10^{-3}$ at 3σ confidence level.

This upper bound imposes a limit on the superradiant growth that in general would lead to transfer up to $\sim\mathcal{O}(10)\%$ of the BH mass into the vector cloud (Brito, Cardoso & Pani 2015a; East & Pretorius 2017; Herdeiro, Radu & Santos 2022). Here we showed that for a field's effective mass of $m_{\rm s} \sim 10^{-19}$ to 10^{-18} eV, the mass of the cloud around Sgr A* cannot exceed the limit $M_{\rm cloud} \lesssim 0.1\%\, M_\bullet$. For a BH spinning with $a/M \sim 0.5$ (an indicative value), the growth time-scale of the cloud can vary between 10^5 and 10^{10} yr, exact values

Table 1. Maximum likelihood estimator $\hat{\Lambda}$ with associated 1σ error and Bayes factors $\log_{10}K$ for different values of α. The measurements for each α are not independent (the same orbit was used to derive them) and therefore cannot be combined to derive a more stringent upper limit. For non-normal distributions we report Λ_1 and Λ_2 defined such that $P(\Lambda_\alpha < \Lambda_1|D) \approx 68\%$ and $P(\Lambda_\alpha < \Lambda_2|D) \approx 99\%$ of $P(\Lambda_\alpha|D)$.

α	$\hat{\Lambda}$	$\log_{10}K$
0.001	$\lesssim(0.51, 0.98)$	−0.45
0.003	0.03596 ± 0.01477	−2.09
0.005	0.00379 ± 0.00157	−3.11
0.008	0.00114 ± 0.00047	1.62
0.01	0.00088 ± 0.00036	1.42
0.02	0.00116 ± 0.00047	1.69
0.03	0.00688 ± 0.00263	−2.55
0.04	0.00617 ± 0.00337	−4.77
0.05	0.00592 ± 0.00339	−4.96

depend on the effective mass m_s. This estimate is below the age of the Universe ($t_{age} \sim 10^{10}$ yr), making the superradiant process and our constraints relevant. In Appendix F, we report the corner plots of two illustrative cases ($\alpha = 0.01$ and $\alpha = 0.001$) to show the correlations between parameters.

3.3 Inclusion of environmental effects

All the above results are obtained neglecting the backreaction effects of the matter on the motion of S2. Indeed, the presence of a matter distribution induces a gravitational drag force on the body moving in it, with the consequence that part of the material is dragged along the motion producing dynamical friction force on the main body (Chandrasekhar 1983; Ostriker 1999). It has been shown that dynamical friction induced by ultralight bosons may play a significant role in the strong regime (Traykova et al. 2021; Vicente & Cardoso 2022). Here we investigated whether dynamical friction affects S2 motion too.

In a Newtonian set-up, including the dynamical friction force means adding the following two components to the equations of motion (Macedo et al. 2013):

$$F_{\mathrm{DF,r}} = F_{\mathrm{DF}}\frac{\dot{r}}{v},$$
$$F_{\mathrm{DF},\phi} = F_{\mathrm{DF}}\frac{r\dot{\phi}}{v}, \tag{20}$$

where $v^2 = \dot{r}^2 + r^2\dot{\phi}^2$, since we have assumed that the motion of S2 happens on the equatorial plane ($\theta = \pi/2$) of the central SMBH.

The term F_{DF} has been derived in Ostriker (1999) for a perturber in linear motion and it reads

$$F_{\mathrm{DF}} = -\frac{4\pi\mu_s^2\rho}{v^2}I_v, \tag{21}$$

with

$$I_v = \begin{cases} \frac{1}{2}\log\left(\frac{1+v/c_s}{1-v/c_s}\right) - \frac{v}{c_s}, & v < c_s, \\ \frac{1}{2}\log\left(1-\frac{c_s^2}{v^2}\right) + \log\left(\frac{vt}{r_{\min}}\right), & v > c_s, \end{cases} \tag{22}$$

where ρ is the density of the matter distribution in equation (5), μ_s is the mass of the star S2 that we take to be $\mu_s = 14\,M_\odot$, and c_s is the speed of sound in the medium that constitutes the environment. Kim & Kim (2007) showed that equation (21) correctly reproduces the results obtained for circular orbits if one substitutes $vt \to 2r(t)$.

Despite the orbit of S2 is far from being circular, we are going to use equation (20) in a first approximation.

We tested four different values of the speed of sound c_s for both the supersonic ($c_s = 10^{-6}$, $c_s = 10^{-3}$) and the subsonic ($c_s = 0.1$, $c_s = 0.03$) regimes, for different values of α. We set $\Lambda = 10^{-3}$, since this corresponds to the maximum allowed value of the fractional mass, but results scale linearly with it.

We found that results are independent of c_s and that the maximum difference in both the astrometry and the radial velocity with respect to the case where no dynamical friction is implemented is always negligible.

In Fig. 5, we report the absolute difference in Dec., RA, and radial velocity in the supersonic case with $c_s = 10^{-3}$. Overall, the effect of dynamical friction is at most 10^{-5} mas in the astrometry and $\approx 10^{-3}$ km s^{-1} in the radial velocity, and in both cases reached around the periastron passages. Overall, it remains well below the current (and future) instrument precision and can be neglected.

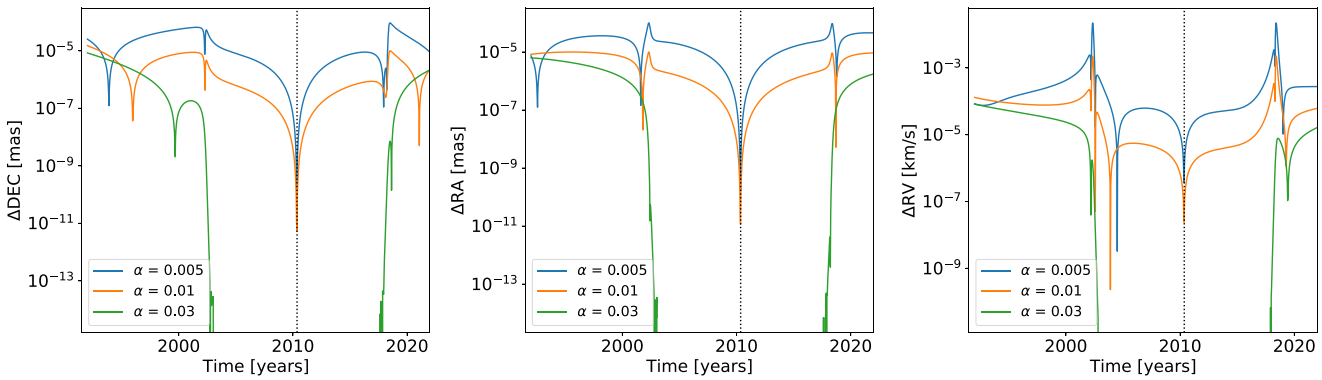

Figure 5. Absolute difference in Dec., RA, and radial velocity between the case where dynamical friction is implemented in the supersonic case with $c_s = 10^{-3}$ and the case where no dynamical friction is present. We set $\Lambda = 10^{-3}$, but results scale linearly with Λ. The difference is maximum around the periastron passages and minimum at the apoastron (black dotted line). Overall, they remain far below the current instrument threshold, whatever the value of α.

We performed the same analysis for the scalar cloud model implemented in Foschi et al. (2023) and the Plummer density profile tested in GRAVITY Collaboration (2022a) too. In both cases, we found similar results to Fig. 5 and hence we conclude that dynamical friction effects can be safely neglected.

Along the same line, one can try to compute the effect that regular gas around Sgr A* has on S2 orbit. In Gillessen et al. (2018), the authors detected a drag force acting on the gas cloud G2 orbiting around Sgr A* and they derived an estimate for the number density of the ambient. Here, we used their same formulation for the drag force, meaning

$$F_{\rm drag} = c_{\rm D} r^{-\gamma} v^2 \mu_{\rm s}, \tag{23}$$

where $\gamma = 1$, v is the relative velocity between the medium and the star that, following Gillessen et al. (2018), is assumed to be equal to the velocity of the star itself, and $c_{\rm D}$ parametrizes the strength of the drag force and it is related to the normalized number density of the gas ambient. In Gillessen et al. (2018), they derived $c_{\rm D} \sim 10^{-3}$, which is the value used in this work as well. In this case, no vector cloud is present ($\Lambda = 0$) and only the force contribution due to the presence of gas is considered.

The maximum difference induced by the drag force exerted by the gas ambient on the astrometry and the radial velocity of S2 is of order $\sim 10^{-6}$ mas and $\sim 10^{-3}$ km s^{-1}, respectively. Hence, also the contribution due to regular gas around Sgr A* has a negligible effect on S2. We also note that the difference induced by the presence of gas is comparable with the effect produced by dynamical friction. Hence, even with the development of future instruments and the advent of GRAVITY+, it will still be hard to disentangle the two effects.

4 CONCLUSIONS

In this paper, we investigated the possibility that a vector cloud of superradiant origin clusters around the SMBH Sgr A*, extending the analysis on scalar clouds performed in Foschi et al. (2023). Specifically, we considered a massive vector field, which gives rise to a spherically symmetric cloud, and in Section 3.1, we investigated the imprints of such a cloud in S2's orbital elements. The MCMC analysis in Section 3.2 confirmed the current upper bound for the fractional mass of $\Lambda \lesssim 0.1\%\, M_\bullet$, recovering previous results on extended masses (GRAVITY Collaboration 2022a; Foschi et al. 2023). Despite the range of field's masses that can be tested with S2 motion is roughly the same in both the scalar and vector cloud case ($10^{-18} \lesssim m_{\rm s} \lesssim 10^{-19}$ eV), in the latter those values can effectively engage a superradiant instability in a time-scale shorter than the cosmic age. This strongly constrains the mass of a possible superradiant cloud at the GC, improving the theoretical bound that can lead to have masses up to two order of magnitude larger (Brito et al. 2015a; East & Pretorius 2017; Herdeiro et al. 2022).

Moreover, the effect of the environment on S2 orbit was also investigated for the first time. We considered both the dynamical friction exerted by the medium on the star, and the effect of ambient gas around Sgr A*. In both cases, the effect on the astrometry and the radial velocity is negligible. This analysis was also extended to the scalar cloud case considered in Foschi et al. (2023) and to the Plummer profile of GRAVITY Collaboration (2022a), showing that even in those cases both effects can be neglected. However, since the difference in the astrometry and the radial velocity induced by those effects is of the same order of magnitude, it will be difficult to separate them even with the advent of future instrumentation.

ACKNOWLEDGEMENTS

GRAVITY is developed in collaboration by MPE, LESIA of Paris Observatory/CNRS/Sorbonne Université/Univ. Paris Diderot and IPAG of Université Grenoble Alpes/CNRS, MPIA, Univ. of Cologne, CENTRA – Centro de Astrofísica e Gravitação, and ESO.

The authors would like to thank the anonymous referee and Jarle Brinchmann for their suggestions that improved this work. We are very grateful to our funding agencies [Max Plank Gesellschaft, European Research Council (ERC), Centre National de la Recherche Scientifique (PNCG, PNGRAM), Deutsche Forschungsgemeinschaft, Bundesministerium für Bildung und Forschung, Paris Observatory (CS, PhyFOG), Observatoire des Sciences de l'Univers de Grenoble, and the Fundação para a Ciência e a Tecnologia], to European Southern Observatory and the Paranal staff, and to the many scientific and technical staff members in our institutions, who helped to make NACO, SINFONI, and GRAVITY a reality. This project has received funding from the European Union's Horizon 2020 Framework Programme under the Marie Sklodowska-Curie grant agreement no. 101007855. We acknowledge the financial support provided by FCT/Portugal through grants 2022.01324.PTDC, PTDC/FIS-AST/7002/2020, UIDB/00099/2020, and UIDB/04459/2020. We acknowledge the funds from the 'European Union NextGenerationEU/PRTR', Programa de Planes Complementarios I+D+I (ref. ASFAE/2022/014).

DATA AVAILABILITY

Publicly available data for astrometry and radial velocity up to 2016.38 can be found in table 5, the electronic version, of Gillessen et al. (2017) at this link: https://iopscience.iop.org/article/10.3847/1538-4357/aa5c41/meta#apjaa5c41t5.

REFERENCES

Abuter R. et al., 2018, A&A, 615, L15
Abuter R. et al., 2023, A&A, 677, L10
Akiyama K. et al., 2022, ApJ, 930, L12
Amaro-Seoane P., Barranco J., Bernal A., Rezzolla L., 2010, J. Cosmol. Astropart. Phys., 11, 002
Arvanitaki A., Dubovsky S., 2011, Phys. Rev. D, 83, 044026
Arvanitaki A., Dimopoulos S., Dubovsky S., Kaloper N., March-Russell J., 2010, Phys. Rev. D, 81, 123530
Bailer-Jones C. A. L., 2017, Practical Bayesian Inference: A Primer for Physical Scientists. Cambridge Univ. Press, Cambridge
Bar N., Blum K., Lacroix T., Panci P., 2019, J. Cosmol. Astropart. Phys., 07, 045
Baryakhtar M., Lasenby R., Teo M., 2017, Phys. Rev. D, 96, 035019
Boshkayev K., Malafarina D., 2019, MNRAS, 484, 3325
Brito R., Cardoso V., Pani P., 2015a, Classical Quantum Gravity, 32, 134001
Brito R., Cardoso V., Pani P., 2015b, Lecture Notes in Physics Vol. 906, Superradiance: Energy Extraction, Black-Hole Bombs and Implications for Astrophysics and Particle Physics. Springer, Cham, Switzerland
Cardoso V., Dias O. J. C., Hartnett G. S., Middleton M., Pani P., Santos J. E., 2018, J. Cosmol. Astropart. Phys., 03, 043
Catanzarite J. H., 2010, preprint (arXiv:1008.3416)
Chandrasekhar S., 1983, The Mathematical Theory of Black Holes. Oxford Univ. Press, Oxford
Chen Y., Xue X., Brito R., Cardoso V., 2023, Phys. Rev. Lett., 130, 111401
De Laurentis M., De Martino I., Della Monica R., 2023, Rep. Prog. Phys., 86, 104901
Della Monica R., de Martino I., 2022, J. Cosmol. Astropart. Phys., 03, 007
East W. E., Pretorius F., 2017, Phys. Rev. Lett., 119, 041101
Endlich S., Penco R., 2017, J. High Energy Phys., 05, 052

Foschi A. et al., 2023, MNRAS, 524, 1075
Genzel R., 2021, preprint (arXiv:2102.13000)
Genzel R., Eisenhauer F., Gillessen S., 2010, Rev. Mod. Phys., 82, 3121
Ghez A. M. et al., 2003, ApJ, 586, L127
Ghez A. M. et al., 2008, ApJ, 689, 1044
Gillessen S., Eisenhauer F., Trippe S., Alexander T., Genzel R., Martins F., Ott T., 2009, ApJ, 692, 1075
Gillessen S. et al., 2017, ApJ, 837, 30
Gillessen S. et al., 2018, preprint (arXiv:1812.01416)
Gondolo P., Silk J., 1999, Phys. Rev. Lett., 83, 1719
Goodsell M., Jaeckel J., Redondo J., Ringwald A., 2009, J. High Energy Phys., 11, 027
GRAVITY Collaboration, 2018, A&A, 618, L10
GRAVITY Collaboration, 2019a, MNRAS, 489, 4606
GRAVITY Collaboration, 2019b, A&A, 625, L10
GRAVITY Collaboration, 2020, A&A, 636, L5
GRAVITY Collaboration, 2022a, A&A, 657, L12
GRAVITY Collaboration, 2022b, A&A, 657, A82
Grould M., Meliani Z., Vincent F. H., Grandclément P., Gourgoulhon E., 2017a, Classical Quantum Gravity, 34, 215007
Grould M., Vincent F. H., Paumard T., Perrin G., 2017b, A&A, 608, A60
Habibi M. et al., 2017, ApJ, 847, 120
Heavens A., Fantaye Y., Mootoovaloo A., Eggers H., Hosenie Z., Kroon S., Sellentin E., 2017, preprint (arXiv:1704.03472)
Heißel G., Paumard T., Perrin G., Vincent F., 2022, A&A, 660, A13
Herdeiro C., Radu E., Rúnarsson H., 2016, Classical Quantum Gravity, 33, 154001
Herdeiro C. A. R., Radu E., Santos N. M., 2022, Phys. Lett. B, 824, 136835
Jaeckel J., Ringwald A., 2010, Annu. Rev. Nucl. Part. Sci., 60, 405
Kass R. E., Raftery A. E., 1995, J. Am. Stat. Assoc., 90, 773
Kim H., Kim W.-T., 2007, ApJ, 665, 432
Kopeikin S., Efroimsky M., Kaplan G., 2011, Relativistic Celestial Mechanics of the Solar System. Wiley-VCH, Weinheim, Germany
Lacroix T., 2018, A&A, 619, A46
Macedo C. F. B., Pani P., Cardoso V., Crispino L. C. B., 2013, ApJ, 774, 48
Marsh D. J. E., 2016, Phys. Rep., 643, 1
Newville M., Stensitzki T., Allen D. B., Rawlik M., Ingargiola A., Nelson A., 2016, Astrophysics Source Code Library, record ascl:1606.014
Ostriker E. C., 1999, ApJ, 513, 252
Pani P., Cardoso V., Gualtieri L., Berti E., Ishibashi A., 2012, Phys. Rev. D, 86, 104017
Plewa P. M. et al., 2015, MNRAS, 453, 3234
Poisson E., Will C., 2012, Gravity: Newtonian, Post-Newtonian, Relativistic. Cambridge Univ. Press, Cambridge
Reid M. J., Brunthaler A., 2020, ApJ, 892, 39
Rosa J. A. L., Garcia P., Vincent F. H., Cardoso V., 2022, Phys. Rev. D, 106, 044031
Sabha N. et al., 2012, A&A, 545, A70
Sadeghian L., Ferrer F., Will C. M., 2013, Phys. Rev. D, 88, 063522
Santos N. M., Benone C. L., Crispino L. C. B., Herdeiro C. A. R., Radu E., 2020, J. High Energy Phys., 07, 010
Schödel R. et al., 2002, Nature, 419, 694
Thorne K. S., 1980, Rev. Mod. Phys., 52, 299
Traykova D., Clough K., Helfer T., Berti E., Ferreira P. G., Hui L., 2021, Phys. Rev. D, 104, 103014
Vicente R., Cardoso V., 2022, Phys. Rev. D, 105, 083008

APPENDIX A: VARIATION OF THE ORBITAL ELEMENTS

The variation of the orbital elements in terms of the perturbing force in equation (8) is given by

$$\frac{\mathrm{d}a}{\mathrm{d}t} = 2\sqrt{\frac{a^3}{M_\bullet(1-e^2)}}\left[e\sin\phi\mathcal{R} + (1+e\cos\phi)\mathcal{S}\right], \tag{A1}$$

$$\frac{\mathrm{d}e}{\mathrm{d}t} = \sqrt{\frac{a(1-e^2)}{M_\bullet}}\left[\sin\phi\mathcal{R} + \frac{2\cos\phi + e(1+\cos^2\phi)}{1+e\cos\phi}\mathcal{S}\right], \tag{A2}$$

$$\frac{\mathrm{d}\omega}{\mathrm{d}t} = \frac{1}{e}\sqrt{\frac{a(1-e^2)}{M_\bullet}}\left[-\cos\phi\mathcal{R} + \frac{1+2e\cos\phi}{1+e\cos\phi}\sin\phi\mathcal{S} - e\cot i\frac{\sin(\omega+\phi)}{1+e\cos\phi}\mathcal{W}\right], \tag{A3}$$

$$\frac{\mathrm{d}i}{\mathrm{d}t} = \sqrt{\frac{a(1-e^2)}{M_\bullet}}\frac{\cos(\omega+\phi)}{1+e\cos\phi}\mathcal{W}, \tag{A4}$$

$$\sin i\frac{\mathrm{d}\Omega}{\mathrm{d}t} = \sqrt{\frac{a(1-e^2)}{M_\bullet}}\frac{\sin(\omega+\phi)}{1+e\cos\phi}\mathcal{W}, \tag{A5}$$

and

$$\frac{\mathrm{d}\mathcal{M}_0}{\mathrm{d}t} = -\sqrt{1-e^2}\left(\frac{\mathrm{d}\omega}{\mathrm{d}t} + \cos i\frac{\mathrm{d}\Omega}{\mathrm{d}t}\right) - \sqrt{\frac{a}{M_\bullet}}\frac{2(e^2-1)}{(1+e\cos\phi)}\mathcal{R}, \tag{A6}$$

where we have used the substitution $r = a(1-e^2)/(1+e\cos\phi)$.

APPENDIX B: INITIAL CONDITIONS AND KEPLER EQUATION

Since we start our numerical integration at apoastron, the six initial conditions for the set of equations in equations (13) can be obtained from the analytical solution of the Keplerian two-body problem, namely

$$r_0 = \frac{a(1-e^2)}{1+e\cos\phi_0}, \qquad \dot{r}_0 = \frac{2\pi e a\sin\mathcal{E}}{P(1-e\cos\mathcal{E})},$$
$$\theta_0 = \frac{\pi}{2}, \qquad \dot{\theta} = 0,$$
$$\phi_0 = 2\arctan\left(\sqrt{\frac{1+e}{1-e}}\tan\frac{\mathcal{E}}{2}\right), \quad \dot{\phi}_0 = \frac{2\pi(1-e)}{P(e\cos\mathcal{E}-1)^2}\sqrt{\frac{1+e}{1-e}}, \tag{B1}$$

where e, a, P are the eccentricity, the semimajor axis, and the period of the orbit, respectively, while $\mathcal{E}$ is the eccentric anomaly evaluated from Kepler's equation: $\mathcal{E} - e\sin\mathcal{E} - \mathcal{M} = 0$, where $\mathcal{M} = \mathcal{M}_0 + n(t-t_\mathrm{p})$ is the mean anomaly, $n = \sqrt{M_\bullet/a^3}$ is the mean angular velocity, and t_p is the time of periastron passage.

Kepler's equation is solved using PYTHON's root finder (scipy.optimize.newton) that implements a Newton–Raphson method. The latter solves the equation with a precision of $\mathcal{O}(10^{-16})$.

APPENDIX C: COORDINATE TRANSFORMATION

The transformation from the orbital reference frame to the observer reference frame can be achieved using the following conversion:

$$\begin{aligned} x' &= Ax_\mathrm{BH} + Fy_\mathrm{BH}, & v_{x'} &= Av_{x_\mathrm{BH}} + Fv_{y_\mathrm{BH}}, \\ y' &= Bx_\mathrm{BH} + Gy_\mathrm{BH}, & v_{y'} &= Bv_{x_\mathrm{BH}} + Gv_{y_\mathrm{BH}}, \\ z_\mathrm{obs} &= -(Cx_\mathrm{BH} + Hy_\mathrm{BH}), & v_{z_\mathrm{obs}} &= -(Cv_{x_\mathrm{BH}} + Hv_{y_\mathrm{BH}}), \end{aligned} \tag{C1}$$

where A, B, C, F, G, and H are the Thiele–Innes parameters (Catanzarite 2010) defined as

$$\begin{aligned} A &= \cos\Omega\cos\omega - \sin\Omega\sin\omega\cos i, \\ B &= \sin\Omega\cos\omega + \cos\Omega\sin\omega\cos i, \\ F &= -\cos\Omega\sin\omega - \sin\Omega\cos\omega\cos i, \\ G &= -\sin\Omega\sin\omega + \cos\Omega\cos\omega\cos i, \\ C &= -\sin\omega\sin i, \\ H &= -\cos\omega\sin i, \end{aligned} \tag{C2}$$

while the Cartesian coordinates $\{x_{\rm BH}, y_{\rm BH}, z_{\rm BH}\}$ and velocities $\{v_{x_{\rm BH}}, v_{y_{\rm BH}}, v_{z_{\rm BH}}\}$ are those obtained from the numerical integration. For a more detailed discussion about how the coordinate system $\{x', y', z_{\rm obs}\}$ and the above transformation are defined, we refer the reader to fig. 1 and appendix B of Gould et al. (2017b).

APPENDIX D: RELATIVISTIC EFFECTS AND RØMER'S DELAY

As said in the main text, there are two main contributions that must be taken into consideration when S2 approaches the periastron: the relativistic Doppler shift and the gravitational redshift. Both of them induce a shift in the spectral lines of S2 that affects the radial velocity measurements. The former is given by

$$1 + z_{\rm D} = \frac{1 + v_{z_{\rm obs}}}{\sqrt{1 - v^2}}, \tag{D1}$$

while the gravitational redshift is defined as

$$1 + z_{\rm G} = \frac{1}{\sqrt{1 - 2M/r_{\rm em}}}. \tag{D2}$$

The two shifts can be combined using equation (D.13) of Gould et al. (2017b) to obtain the total radial velocity,

$$V_{\rm R} \approx \frac{1}{\sqrt{1-\epsilon}}\,\frac{1 + v_{z_{\rm obs}}/\sqrt{1-\epsilon}}{\sqrt{1 - v^2/(1-\epsilon)}} - 1, \tag{D3}$$

where $\epsilon = 2M/r_{\rm em}$.

In the total space velocity $v = |\boldsymbol{v}|$ we must also add a correction due to the Solar system motion. We followed the most recent work of Reid & Brunthaler (2020) and take a proper motion of Sgr A∗ of

$$\begin{aligned} v_x^{\rm SSM} &= -5.585\,{\rm mas\,yr^{-1}} = 6.415\cos(209.^\circ47)\,{\rm mas\,yr^{-1}}, \\ v_y^{\rm SSM} &= -3.156\,{\rm mas\,yr^{-1}} = 6.415\sin(209.^\circ47)\,{\rm mas\,yr^{-1}}. \end{aligned} \tag{D4}$$

The Rømer's delay is instead included using the first-order Taylor's expansion of the Rømer's equation $t_{\rm obs} - t_{\rm em} - z_{\rm obs}(t_{\rm em}) = 0$, which reads

$$t_{\rm em} = t_{\rm obs} - \frac{z_{\rm obs}(t_{\rm obs})}{1 + v_{z_{\rm obs}}(t_{\rm obs})}. \tag{D5}$$

The difference between the exact solution and the approximated one in equation (D5) is at most ∼4 s over S2 orbit and therefore negligible. The Rømer effect affects both the astrometry and the spectroscopy, with an impact of ≈450 μas on the position and ≈50 km s^{-1} at periastron for the radial velocity. Our results recover the previous estimates for this effect in Gould et al. (2017b) and Abuter et al. (2018).

Table E1. Uniform priors used in the MCMC analysis. Initial guesses Θ_i^0 coincide with the best-fitting parameters found by MINIMIZE.

Parameter	Θ_i^0	Lower bound	Upper bound
e	0.88441	0.83	0.93
$a_{\rm sma}$ (as)	0.12497	0.119	0.132
$i_{\rm orb}$ (°)	134.69241	100	150
$\omega_{\rm orb}$ (°)	66.28411	40	90
$\Omega_{\rm orb}$ (°)	228.19245	200	250
$t_{\rm p}$ (yr)	2018.37902	2018	2019
$M_\bullet$ (10^6 M$_\odot$)	4.29950	4.1	4.8
R_0 (10^3 pc)	8.27795	8.1	8.9
Λ	0.001	0	1

Table E2. Gaussian priors used in the MCMC analysis. Initial guesses Θ_i^0 coincide with the best-fitting parameters found by MINIMIZE. ξ and σ represent the mean and the standard deviation of the distributions, respectively, and they come from Plewa et al. (2015).

Parameter	Θ_i^0	ξ	σ
x_0 (mas)	−0.244	−0.055	0.25
y_0 (mas)	−0.618	−0.570	0.15
v_{x_0} (mas yr^{-1})	0.059	0.063	0.0066
v_{y_0} (mas yr^{-1})	0.074	0.032	0.019
v_{z_0} (km s^{-1})	−2.455	0	5

APPENDIX E: MCMC DETAILS

We used a Gaussian log-likelihood given by

$$\ln\mathcal{L} = \ln\mathcal{L}_{\rm pos} + \ln\mathcal{L}_{\rm vel}, \tag{E1}$$

where

$$\ln\mathcal{L}_{\rm pos} = -\sum_{i=1}^{N}\left[\frac{({\rm Dec.}_i - {\rm Dec.}_{{\rm model},i})^2}{\sigma^2_{{\rm Dec.}_i}} + \frac{({\rm RA}_i - {\rm RA}_{{\rm model},i})^2}{\sigma^2_{{\rm RA}_i}}\right] \tag{E2}$$

and

$$\ln\mathcal{L}_{\rm vel} = -\sum_{i=1}^{N}\frac{(V_{{\rm R},i} - V_{{\rm model},i})^2}{\sigma^2_{V_{{\rm R},i}}}. \tag{E3}$$

The priors we used are listed in Table E1-E2. We used uniform priors for the physical parameters, i.e. we only imposed physically motivated bounds and Gaussian priors for the additional parameters describing NACO data, since the latter have been well constrained by previous work (Plewa et al. 2015) and are not expected to change.

The initial points Θ_i^0 in the MCMC are chosen such that they minimize the χ^2 when $f_{\rm SP} = 1$ and $\Lambda = 0$. The minimization is performed using the PYTHON package LMFIT.MINIMIZE (Newville et al. 2016) with the Levenberg–Marquardt method.

In the sampling phase of the MCMC implementation, we used 64 walkers and 10^5 iterations. Since we started our MCMC at the minimum found by MINIMIZE, we skipped the burning-in phase and we used the last 80 per cent of the chains to compute the mean and standard deviation of the posterior distributions. The convergence of the MCMC analysis is assured by means of the autocorrelation time $\tau_{\rm c}$, i.e. we ran N iterations such that $N \gg 50\,\tau_{\rm c}$.

APPENDIX F: CORNER PLOTS

Here, we report the corner plots for two representative values of α ($\alpha = 0.01$ in Figure F1 and $\alpha = 0.001$ in Figure F2) to show

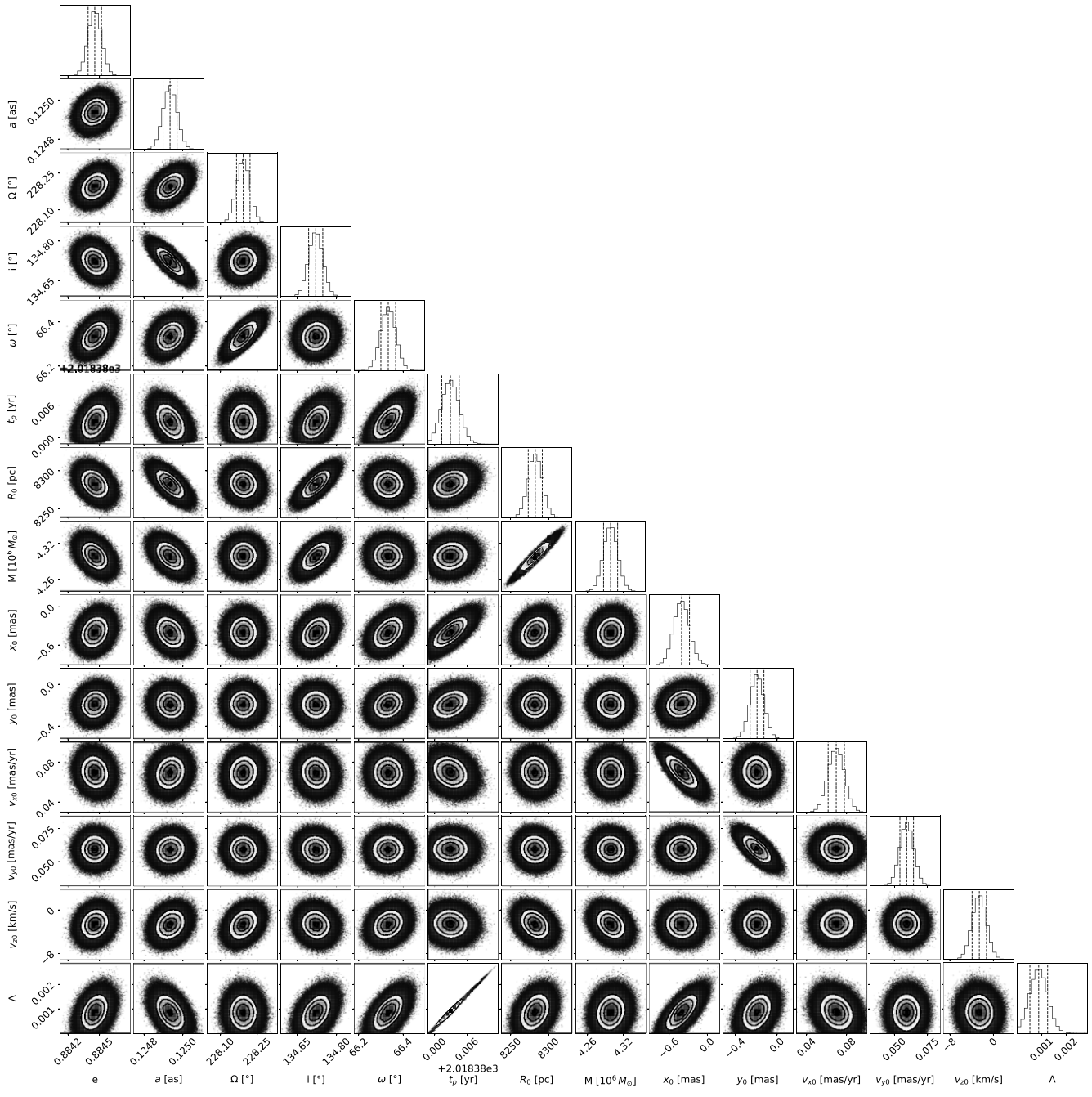

Figure F1. Corner plot of the fitted parameters with $f_{\rm SP} = 1$ and $\alpha = 0.01$. Dashed lines represent the 0.16, 0.50, and 0.84 quantiles of the distributions.

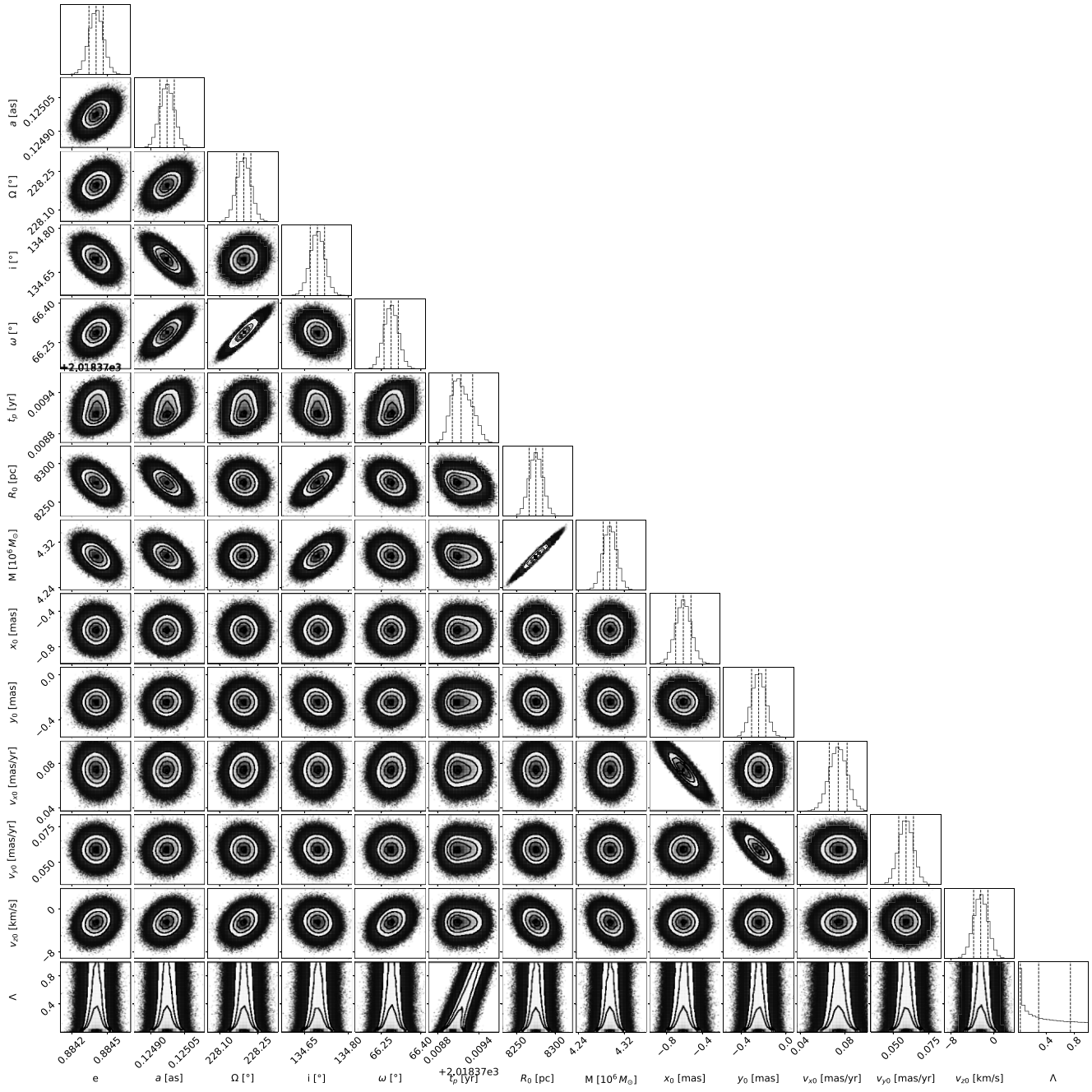

Figure F2. Corner plot of the fitted parameters with $f_{SP} = 1$ and $\alpha = 0.001$. Dashed lines represent the 0.16, 0.50, and 0.84 quantiles of the distributions.

the behaviour of the parameters when the cloud is located in and outside S2's orbital range. The strong correlation between Λ and the periastron passage t_p when $\alpha = 0.01$ can be understood following the argument of Heißel et al. (2022): the presence of an extended mass will induce a retrograde precession in the orbit that will result in a positive shift of the periastron passage time, needed to compensate the (negative) shift in the initial true anomaly. Indeed, when considering the Schwarzschild precession, which instead induces a prograde precession (hence a positive initial shift in the true anomaly), t_p will undergo a negative shift, as can be seen from the strong anticorrelation between f_{SP} and t_p reported in GRAVITY Collaboration (2020).

[1]*CENTRA – Centro de Astrofísica e Gravitação, IST, Universidade de Lisboa, P-1049-001 Lisboa, Portugal*
[2]*Faculdade de Engenharia, Universidade do Porto, Rua Dr Roberto Frias, P-4200-465 Porto, Portugal*
[3]*European Southern Observatory, Karl-Schwarzschild-Straße 2, D-85748 Garching, Germany*
[4]*LESIA, Observatoire de Paris, Université PSL, CNRS, Sorbonne Université, Université de Paris, 5 place Jules Janssen, F-92195 Meudon, France*
[5]*Max Planck Institute for extraterrestrial Physics, Giessenbachstraße 1, D-85748 Garching, Germany*
[6]*Universitat Politècnica de València, València, Spain*
[7]*Kavli Institute for Astronomy and Astrophysics, Beijing, China*
[8]*Higgs Centre for Theoretical Physics, Edinburgh, UK*

[9]*Universidade de Lisboa – Faculdade de Ciências, Campo Grande, P-1749-016 Lisboa, Portugal*
[10]*Univ. Grenoble Alpes, CNRS, IPAG, F-38000 Grenoble, France*
[11]*Max Planck Institute for Astronomy, Königstuhl 17, D-69117 Heidelberg, Germany*
[12]*Leiden University, NL-2311 EZ Leiden, the Netherlands*
[13]*Institute of Astronomy, KU Leuven, Celestijnenlaan 200D, B-3001 Leuven, Belgium*
[14]*Department of Astrophysical and Planetary Sciences, JILA, University of Colorado Boulder, Duane Physics Bldg, 2000 Colorado Ave, Boulder, CO 80309, USA*
[15]*1st Institute of Physics, University of Cologne, Zülpicher Straße 77, D-50937 Cologne, Germany*
[16]*Max Planck Institute for Radio Astronomy, Auf dem Hügel 69, D-53121 Bonn, Germany*
[17]*Departments of Physics and Astronomy, University of California, Le Conte Hall, Berkeley, CA 94720, USA*
[18]*European Southern Observatory, Casilla 19001, Santiago 19, Chile*
[19]*Advanced Concepts Team, European Space Agency, TEC-SF, ESTEC, Keplerlaan 1, NL-2201 AZ Noordwijk, the Netherlands*
[20]*Université Côte d'Azur, Observatoire de la Côte d'Azur, CNRS, Lagrange, France*
[21]*Max Planck Institute for Astrophysics, Karl-Schwarzschild-Straße 1, D-85748 Garching, Germany*

This paper has been typeset from a TEX/LATEX file prepared by the author.